Electronic Supplementary Material (ESI) for Inorganic Chemistry Frontiers.

Supporting Information for

Maximizing the catalytic performance of FER zeolite in the methanol-to-hydrocarbon process by manipulating crystal size and constructing bifunctionality

Xin Zhang, Hexun Zhou, Yiru Ye, Xinyu You, Xue Zhou, Shican Jiang, Kun Liu, Abhishek Dutta Chowdhury

S1. Experimental section

S1.1. Materials

Commercial FER zeolite (ZSM-35, SiO_2/Al_2O_3=25, H type) was purchased from the Catalyst Plant of Nankai University (Tianjin, China) and donated as c-FER in this work. Yttrium oxide (Y_2O_3, 99%) was purchased from Shanghai yuanye Bio-Technology Co., Ltd. Flake shape FER zeolite (denoated as f-FER in this work) was synthesized by the hydrothermal method using ethylene glycol (EG, 99%, Aldrich) as organic structure directing agent (OSDA).[1,2] Sodium hydroxide (NaOH, AR, Sinopharm), H_2O, sodium aluminate ($NaAlO_2$, AR, Macklin), and EG were mixed in a particular order. After stirring for 30 min, colloidal silica (LUDOX AS-40, 40 wt %, Aldrich) and glucose (AR, Sinopharm) were added into the liquid, forming the suspension with chemical composition: 0.12 Na_2O: 1 SiO_2: 7 EG: 0.033 Al_2O_3: 0.1 glucose: 20 H_2O. The precursor suspension was stirred for 30 min and then aged for 18 h on an orbital shaker. The aged precursor was then transferred into a 50 mL Teflon-lined autoclave and dynamically crystallyzed at 180 ^oC for 48 h. The obtained solid was washed and dried overnight at 110 ^oC and then calcined in air at 550 ^oC for 6 h. The calcined samples were ion-exchanged thrice with 1 M NH_4Cl solutions and finally obtained H-type zeolite material.

S1.2. Methods and characterization

Powder X-ray diffraction (XRD) patterns were conducted with a German Bruker D8 Advance diffractometer using Cu Kα radiation. The data was collected in a 2θ range of 5-60^o

using a step size of 0.02º and a scan speed of 2º·min^{-1}. N_2 physisorption measurement was performed on an automated gas sorption system Micromeritics ASAP 2460 instrument. The samples were degassed under vacuum for 10 h at 573 K before the measurement. The total surface areas were obtained based on the BET equation, while the micropore volumes and micropore surface areas were evaluated using the t-plot method. The elemental contents of samples were analyzed on an inductively coupled plasma optical emission spectroscopy (ICP-OES). The crystal morphologies were observed using a scanning electron microscope (Hitachi-SU8010, Japan). Temperature-programmed desorption of ammonia (NH_3-TPD) was measured on a MicrotracBEL (BELCAT-B, Japan) chemical adsorption instrument. Each sample (50mg) was loaded into a quartz reactor and pre-treated at 823 K for 1 h in flowing He. After the pretreatment, the sample was cooled to 373 K for 30 minutes and saturated with NH_3 gas. Then, NH_3-TPD was carried out in a constant flow of He (30 mL·min^{-1}) from 323 K to 1023 K at a heating rate of 10 K·min^{-1}. Brønsted and Lewis acid site concentrations of FER zeolites were investigated by studying pyridine adsorption on a FTIR spectrometer (Thermo IS50). The samples were put into the cell and pretreated at 450 ºC under vacuum for 1 h to remove impurities. After cooling to 30 ºC, the cell was scanned, and obtained data were used as background. Then pyridine was adsorbed at 30 ºC to reach equilibrium. Then the cell was vacuumed for 30 min to remove excess pyridine. The desorption spectrum was obtained by scanning IR when the cell was heated at 150 ºC and 250 ºC, respectively. Spectra were recorded in the 1400-1700 cm^{-1} range at a resolution of 4 cm^{-1} and co-addition of 64 scans. The following formulas were used to quantify the Brønsted (BAS) and Lewis acid sites (LAS):[3]

$$C_{BAS} = 1.88 \times \mathrm{I}_B \times \mathrm{R}^2/\mathrm{W}$$

$$C_{LAS} = 1.42 \times \mathrm{I}_L \times \mathrm{R}^2/\mathrm{W}$$

Where I_B and I_L are the integrated absorbance of BAS and LAS, respectively. R is the radius of catalyst disk (cm), and W is the mass of catalyst (mg).

^{27}Al MAS NMR spectra were recorded at a spinning rate of 15 kHz using one pulse sequence with 4 mm CPMAS probe, 4k scans were accumulated, with a π/12 pulse width of 0.312 μs and a 1 s recycle delay, where chemical shifts were externally referenced to Al $(NO_3)_3$ (liquid).

S1.3. Catalytic testing

Methanol-to-hydrocarbons (MTH) reactions were performed in a fixed-bed reactor (Xiamen Hande Engineering Co., Ltd.) with a 10 mm inner diameter quartz tubular reactor. The calcined zeolite catalysts were pelletized and crushed into 45-110 mesh, and the obtained catalysts (0.5 g) were mixed with SiC (3 g) at a weight ratio of 1:6 (catalyst/SiC). Before the reaction, the catalytic bed was pretreated with Argon at 550 °C for 2 h. After pretreatment, the temperature decreased to reaction temperature (400-500 °C), and WHSV was set from 4.0~0.5 h^{-1}, with methanol being diluted in Ar to a constant molar MeOH/Ar ratio of 1:2 at a pressure of 1 bar. Intra-mixed samples were prepared by physically mixing FER zeolite powders with Y_2O_3 powders using an agate mortar and pestle and pelletizing, crushing, and sieving to obtain 45-110 mush aggregates. Inter-mixed mixtures were prepared by mixing individually prepared 45-110 mush aggregates of FER zeolites with 45-110 mush aggregates of Y_2O_3. All the mass

ratio of zeolite/Y_2O_3 is 1:1. The reaction products were analyzed online using gas chromatography (GC-8850, Lunan Ruihong Co., Ltd.) with three detectors: two flame ionization detectors (FIDs) and one thermal conductivity detector (TCD). The permanent gas (Ar, N_2, CH_4, CO, and CO_2) was detected by TCD through GDX-104 and TDX-101 columns. The separation of methanol, dimethoxy ether (DME), and C_1−C_4 hydrocarbons was carried out on a KB-PLOT Q column (30m*0.53mm*40um), while the separation of C_{5+} hydrocarbons was carried out on a KB-5 column (60m*0.32mm*1.0um). Methanol conversion (X, %) and selectivity (S, %) of each product are defined as follows:

$$X = \frac{n_{C,MeOH_{in}} - n_{C,MeOH_{out}} - 2 \cdot n_{C,DME_{out}}}{n_{C,MeOH_{in}}} \cdot 100\% \quad (1)$$

$$S_i = \frac{i \cdot n_{Ci}}{n_{C,MeOH_{in}} - n_{C,oxy_{out}}} \cdot 100\% \quad (2)$$

S1.4. Operando UV-Vis Diffuse Reflectance Spectroscopy (DRS) Study Coupled with Online Mass Spectrometry (MS)

All the catalytic operando studies were performed using a Linkam cell (THMS600) equipped with a temperature controller (Linkam TMS94), and its lid was equipped with a quartz window compatible with UV-Vis detection (See Fig. S1 for the details of our set-up). The UV-Vis diffuse reflectance spectroscopy (DRS) measurements were performed with an AvaSpec-ULS2048L-USB2-UA-RS micro-spectrophotometer from Avantes (see https://www.avantes.com/products/spectrometers/starline/avaspec-uls2048cl-evo/). Halogen

and deuterium lamps were used together for illumination. The online gas phase product analyses were performed by Pfeiffer OmniStar GSD 350 O3 (1-200 amu) mass spectrometer, which was directly connected to the outlet of the Linkam cell. The National Institute of Standards and Technology (NIST) mass spectrometry database was consulted for assignment and referencing purposes. Herein, the signals identified at 26 amu, 30 amu, 41 amu, 43 amu, 54 amu, 56 amu, 67 amu, and 70 amu were attributed to ethylene, formaldehyde, propylene, butyl-, butadiene, butene, pentadiene and pentene, respectively.[4–6] Due to the overlapping of certain intermediates with the reactant methanol or other effluent species, the secondary base peak was considered for identifying formaldehyde and butadiene. In contrast, other species were corroborated by their highest intense primary base peaks.[7,8] During operando studies, all reactions were performed without pressing and sieving the zeolite materials. Operando UV-Vis DRS reactions were performed using ca. 40 mg of the catalyst material. Initially, it was placed on the heating stage of the Linkam cell, which was further connected to a water cooler. The inlet of the cell was connected to the N_2 gas line, via a liquid saturator (containing ^{12}C-methanol (MeOH, AR, Sinopharm Chemical Co. Ltd.) or ^{13}C-methanol (99 atom % ^{13}C, Cambridge Isotope Laboratories). The outlet was either connected to the Pfeiffer mass spectrometer or vented out. The lid of the Linkam cell is equipped with a quartz window to monitor the reaction by UV-vis DRS. Before each UV-vis DRS, the material was further pre-treated/activated according to the following procedure under an N_2 environment (flow rate of 20 ml/min): heating to 673 K at 10 K/min and keeping the sample at this temperature for the next 10 min; then, heating the sample to 823 K at a rate of 5 K/min and hold there for the next 30 min. Next,

the sample was cooled down to the reaction temperature with a rate of 10 K/min under a flow of N_2 gas (flow rate of 20 ml/min). The starting time of the reaction was considered when the inward N_2 flow goes through the liquid saturator. Finally, the reaction was quenched by rapidly cooling the Linkam cell using a Linkam TMS94 temperature controller. During these experiments, the UV-vis DRS was recorded every 15 s intervals during the MTH experiment, which typically took 20 min. The Operando UV-vis spectra were collected every minute, with 300 accumulations of 50 ms exposure time each. Other relevant details are mentioned in the figure captions.

S1.5. Solid-state nuclear magnetic resonance study on spent ^{13}C-enriched zeolite catalysts

All ^{1}H and ^{13}C related (both 1D and 2D) magic angle spinning (MAS) solid-state nuclear magnetic resonance (ssNMR) spectroscopic experiments were performed on Bruker AVANCE NEO spectrometers operating at 400 MHz frequency for ^{1}H using a 4 mm CPMAS H/X/Y probe (CP: Cross-polarization). NMR chemical shifts are reported with respect to the external reference adamantane. Herein, samples were prepared using fully enriched $^{13}CH_3OH$ at our typical experimental conditions (as discussed in the previous section) to increase the solid-state NMR sensitivity. All NMR measurements were performed at room temperature (298 K) and the magic angle spinning rate was set to 10 kHz. Note that effective sample temperatures can be 5-10 degrees higher due to frictional heating. The 1D ^{1}H-^{13}C CP/MAS NMR experiments

were recorded using a 2.0 s recycle delay, an 18 ms acquisition time, and an accumulation of 2000 scans. The Hartmann-Hahn condition was achieved using hexamethylbenzene (HMB), with a contact time of 3000 μs. The 2D ^{13}C-^{13}C PDSD (proton-drive-spin-diffusion) spectra were recorded at 10 kHz MAS, a 70% ramp for the ^{1}H CP pulse with a 3000 μs CP contact time, 2 s recycle delay, 15 ms and 10 ms acquisition times for direct and indirect ^{13}C dimensions, respectively. The 2D ^{13}C-^{1}H CP HETCOR spectra used a ^{1}H $\pi/2$ pulse width of 4.51 μs. The cross-polarization step was performed using a contact time of 3000 μs. A total of 320 t1 FIDs were recorded at increments of 20 ms using the States-TPPI method to achieve sign discrimination in F1. ^{1}H SPINAL-64 decoupling was applied during the t2 acquistion with a RF-field amplitude of 55kHz. In all cases, other relevant acquisitions/experimental parameters were described in figure captions. All NMR spectra were processed and analyzed using Bruker TopSpin 4.2.

S2. Supplementary Tables and Figures

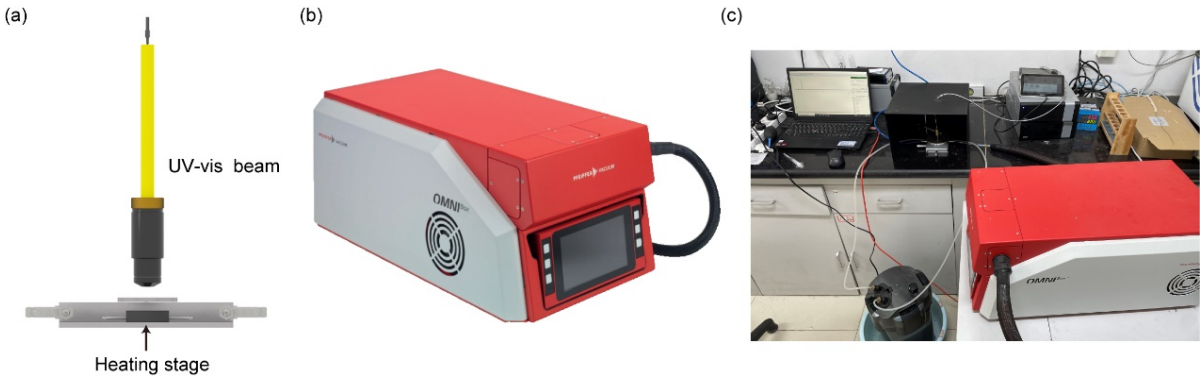

Fig. S1 The operando set-up consists of UV-Vis diffuse reflectance spectroscopy (UV-Vis DRS) coupled with online mass spectrometry (MS): (a) Illustration of the UV-vis DRS working principle along with images of (b) online MS, and (c) the whole working set-up. See experimental Section S1.4 for the technical details.

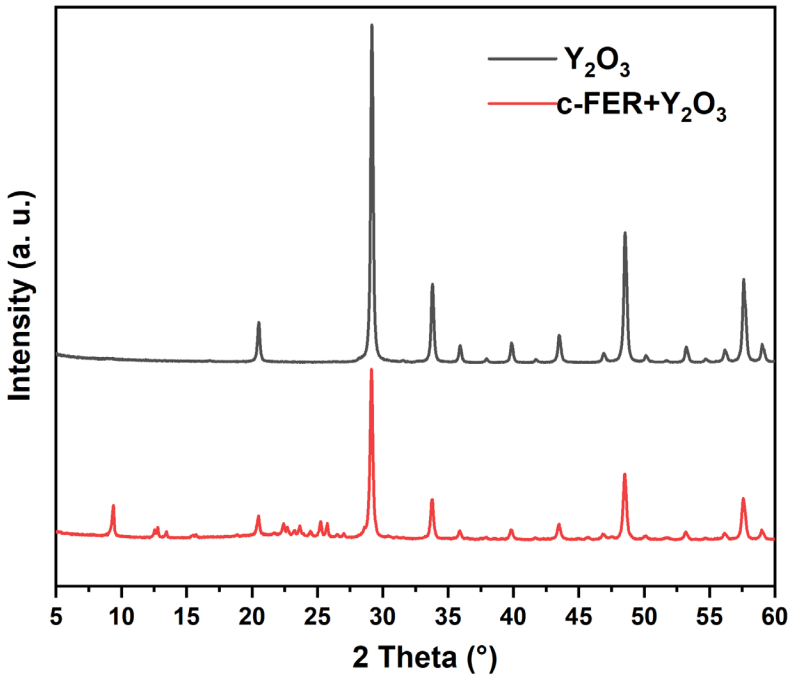

Fig. S2 XRD pattern of standalone Y_2O_3 and bifunctional (c-FER+Y_2O_3) systems. The Y_2O_3 used in this study has high crystallinity and does not affect the structure of c-FER.

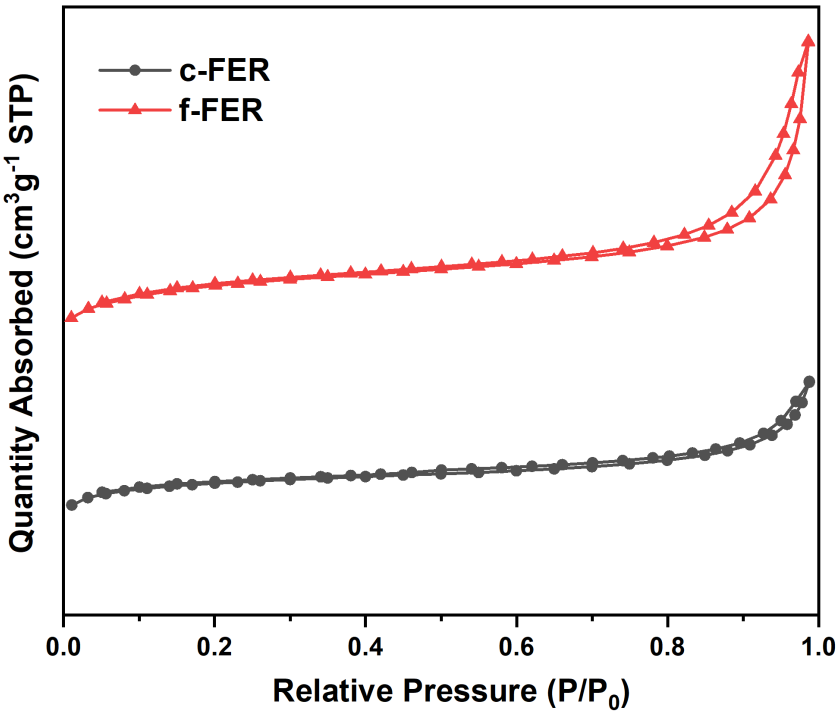

Fig. S3 N_2 sorption isotherms of c-FER and f-FER zeolites used in this study.

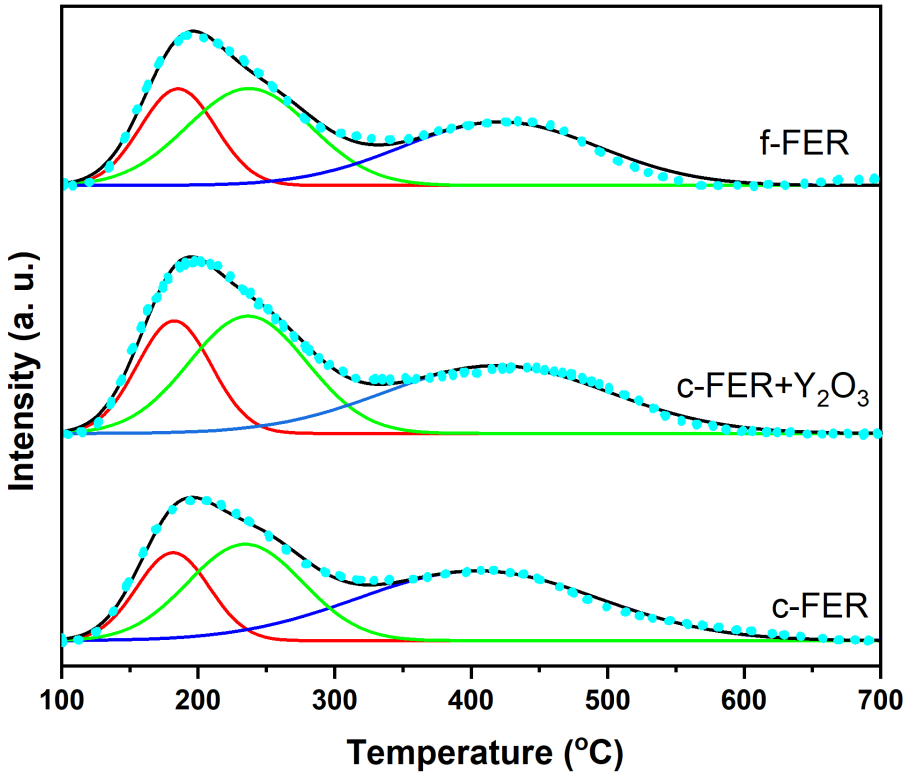

Fig. S4 NH_3-TPD profile of standalone c-FER and f-FER zeolites as well as bifunctional (c-FER+Y_2O_3) systems.

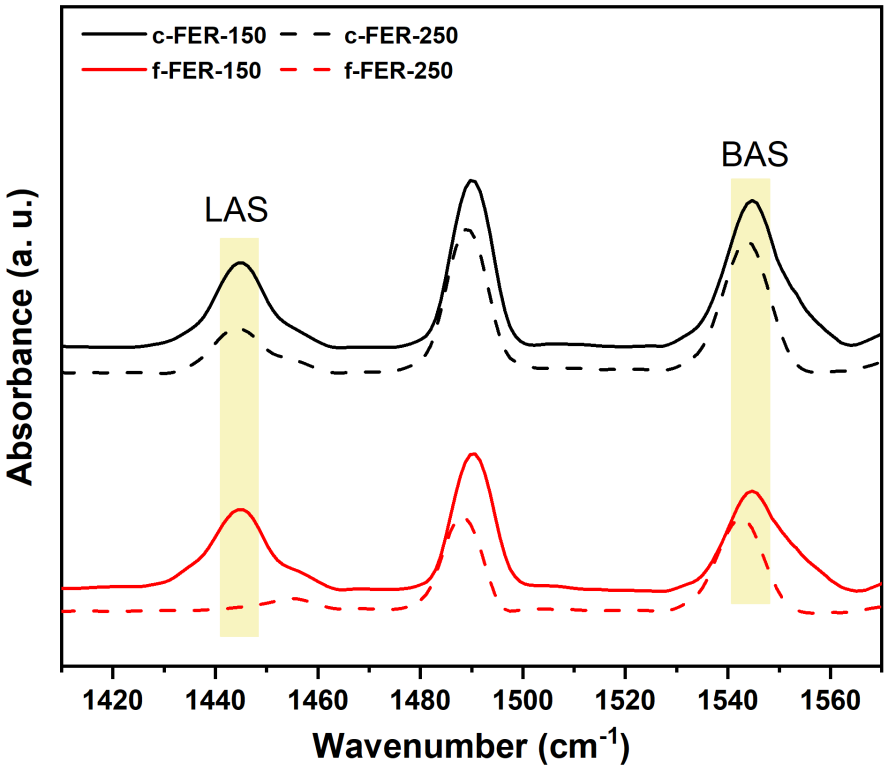

Fig. S5 FTIR spectra of standalone c-FER and f-FER zeolites after exposure to pyridine, measured at two different temperatures (150 ^{O}C and 250 ^{O}C). Spectra showing bands at 1540 cm^{-1} and 1450 cm^{-1} characterizing Brønsted and Lewis acid sites, respectively (see Table S2 for more details).

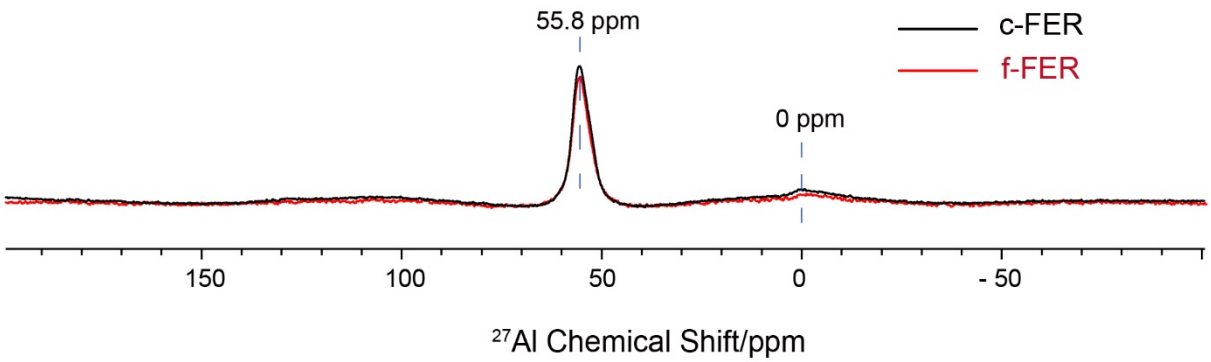

Fig. S6 1D ^{27}Al magic angle spinning (MAS, 15 KHz) solid-state NMR spectra of standalone c-FER and f-FER zeolites.

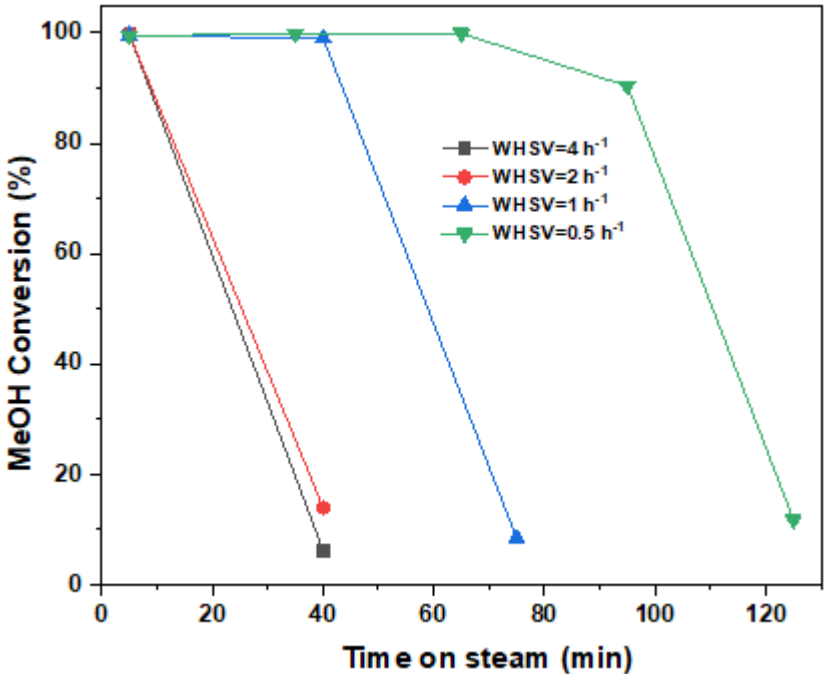

Fig. S7 Methanol conversion at 400 °C under 4-0.5 h^{-1} WHSV over standalone monofunctional c-FER zeolites.

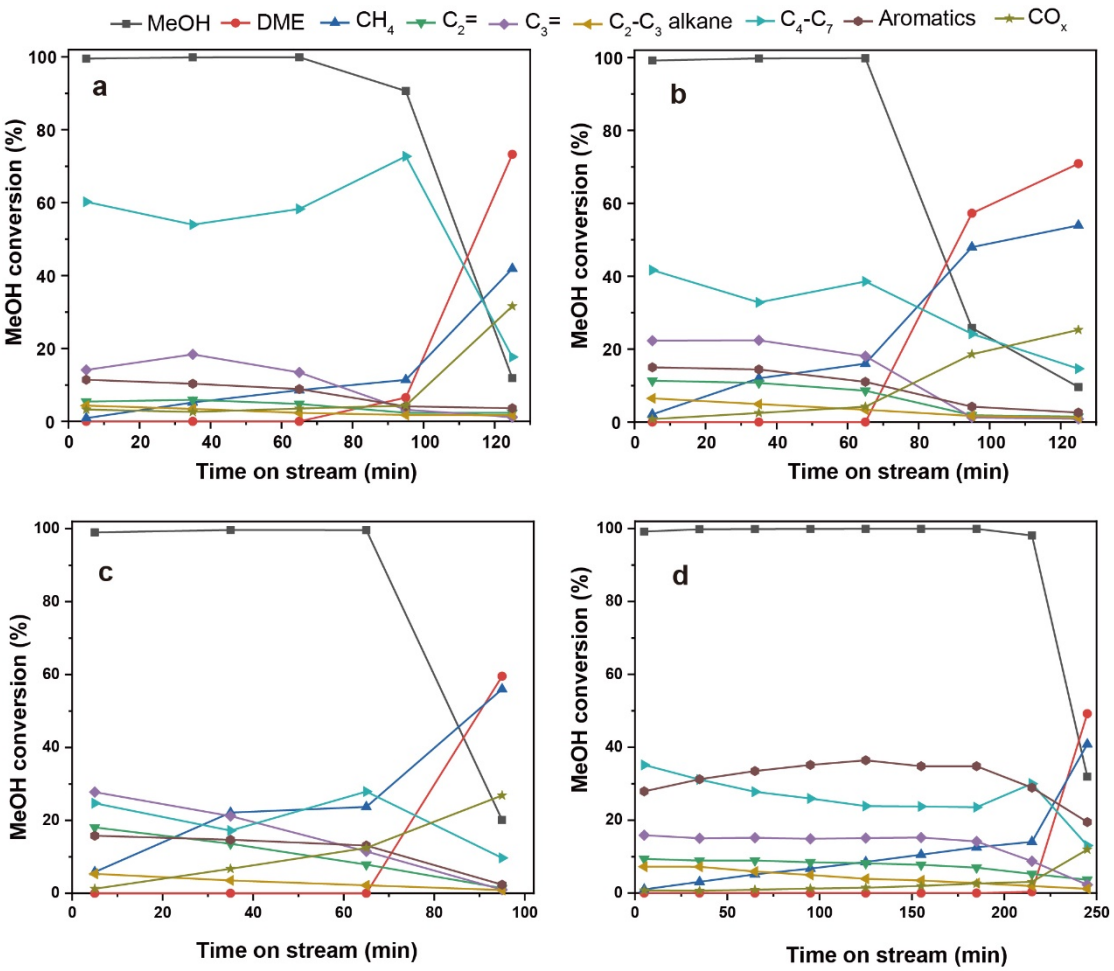

Fig. S8 The MTH catalytic performance evaluation over standalone monofunctional (a-c) c-FER and (d) f-FER zeolites: Methanol conversion and products selectivity over standalone c-FER zeolites at (a) 400 °C, (b) 450 °C, and (c) 500 °C, and (d) f-FER at 450 °C under 0.5 h^{-1} WHSV.

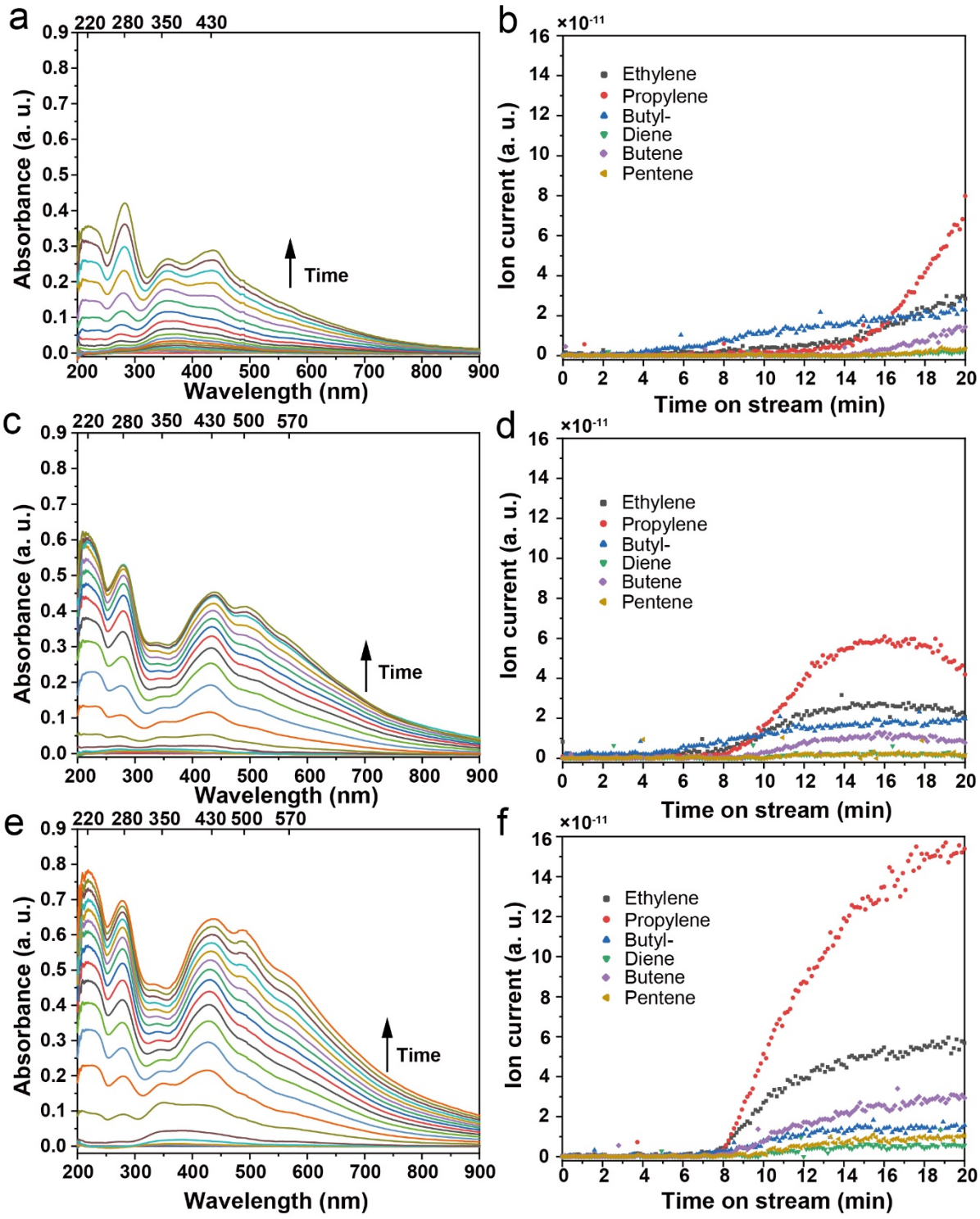

Fig. S9 The operando UV-vis spectroscopy and mass-spectral profiles of methanol conversion over standalone monofunctional c-FER under 400 ºC (a, b), 450 ºC (c, d), and 500 ºC (e, f) for 20 min.

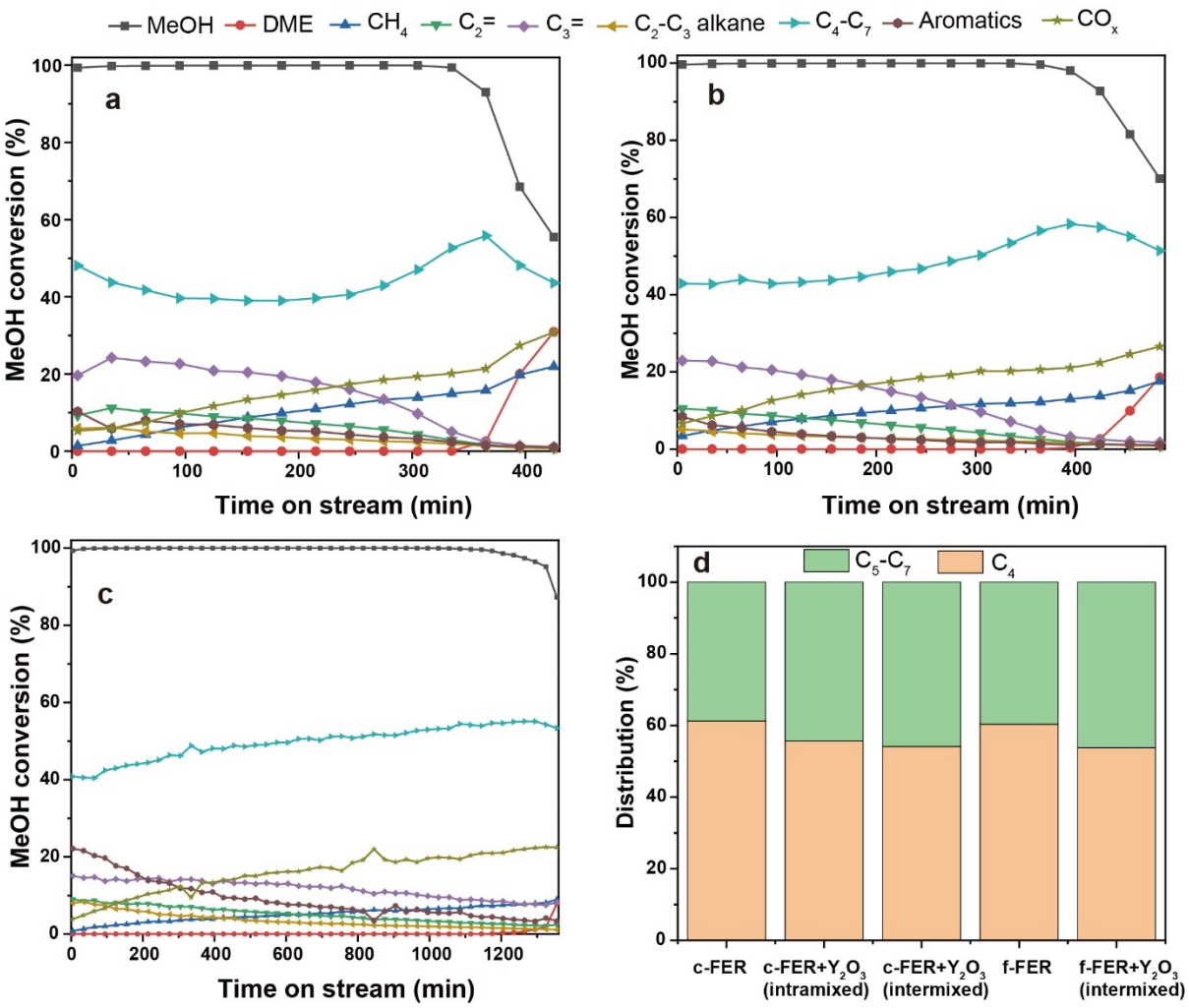

Fig. S10 The MTH catalytic performance evaluation over bifunctional c-FER and f-FER zeolites mixed with Y_2O_3: Methanol conversion and products selectivity over bifunctional (a) c-FER+Y_2O_3-intramixed, (b) c-FER+Y_2O_3-intermixed and (c) f-FER+Y_2O_3-intermixed systems, at 450 ^oC under 0.5 h^{-1} WHSV; and (d) the relative fraction of C_4-hydrocarbons among the gasoline-ranged C_4-C_7 hydrocarbons over different catalytic systems.

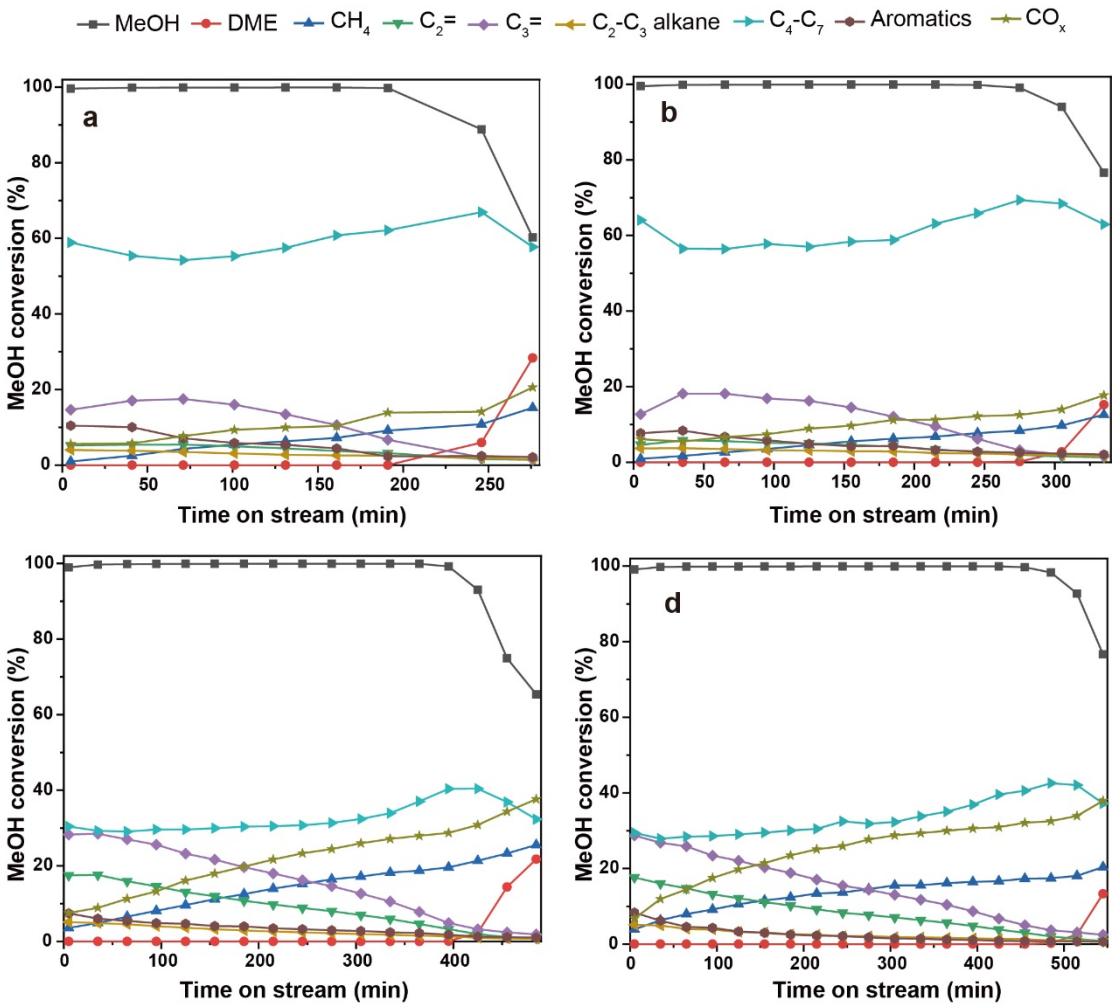

Fig. S11 The MTH catalytic performance evaluation over bifunctional c-FER zeolite mixed with Y_2O_3: Methanol conversion and products selectivity of (a) c-FER+Y_2O_3-intramixed at 400 °C, (b) c-FER+Y_2O_3-intermixed at 400 °C, (c) c-FER+Y_2O_3-intramixed at 500 °C, and (d) c-FER+Y_2O_3-intermixed at 500 °C. WHSV=0.5 h^{-1}.

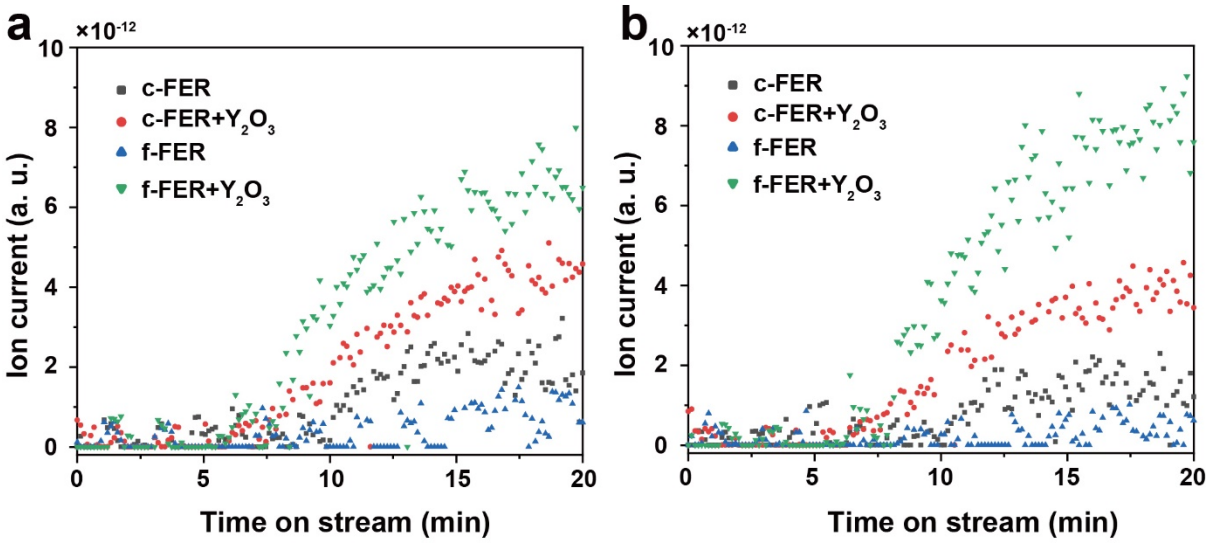

Fig. S12 Mass spectra profiles of butadiene (a) and pentadiene (b) over monofunctional c-FER, f-FER, and bifunctional c-FER+Y_2O_3, f-FER+Y_2O_3 systems. This observation suggests that the co-addition of Y_2O_3 does not greatly impact the diene formation, implying that the olefin-induced hydrogen transfer pathway is still operating.[9,10] It also essentially means that the bifunctional system primarily diminishes the efficiency of methanol-induced hydrogen transfer activities.

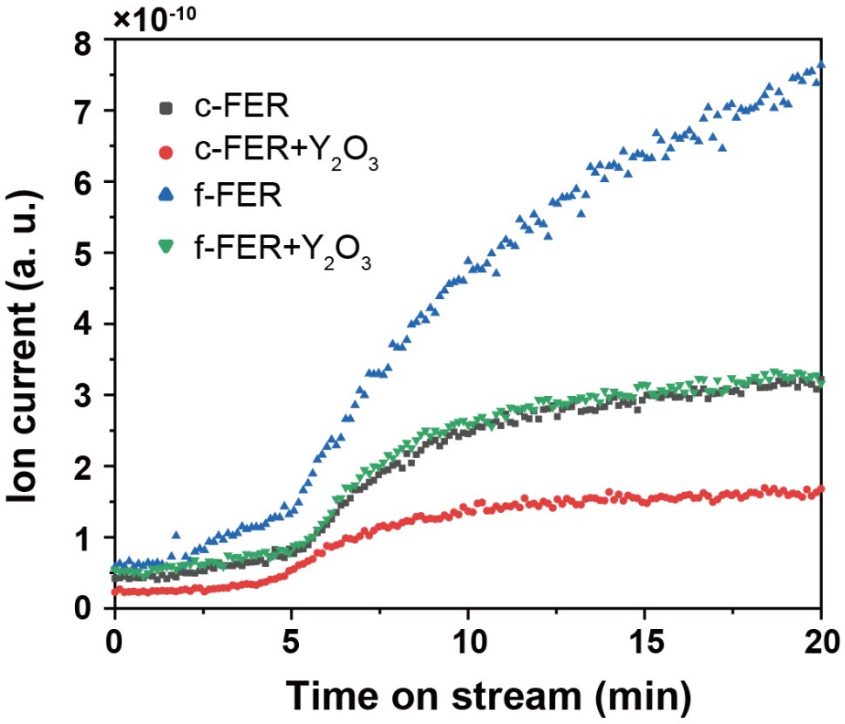

Fig. S13 Mass spectra profiles of HCHO over monofunctional c-FER, f-FER, and bifunctional c-FER+Y_2O_3, f-FER+Y_2O_3 systems. This observation suggests that the co-addition of Y_2O_3 significantly impacts the formation of HCHO during the early phases of the MTH reaction, where Y_2O_3 acts as an HCHO scavenger.[11] The relatively higher content of HCHO over our f-FER systems could be linked to the somewhat higher aromatics selectivity compared to c-FER-led systems.

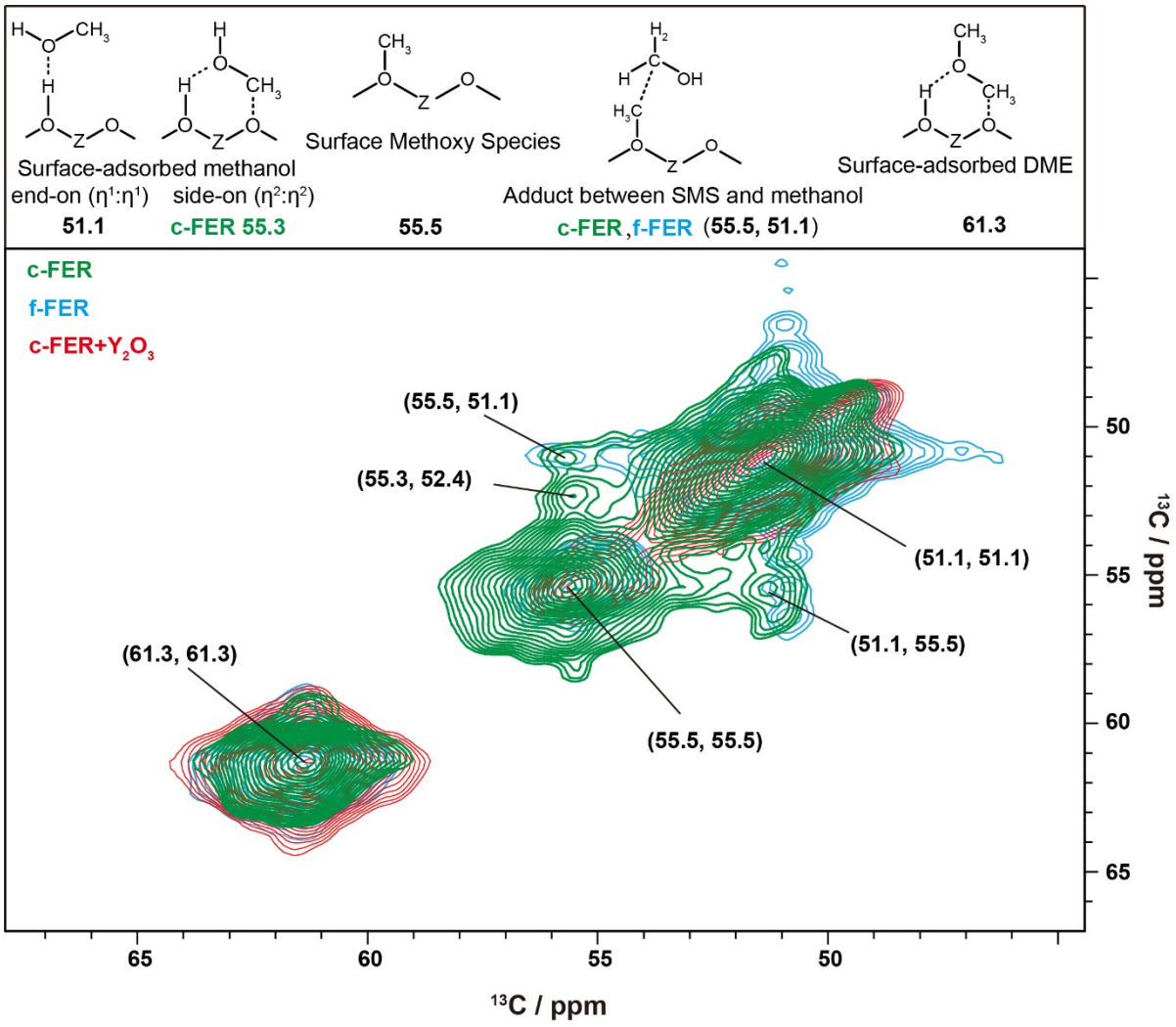

Fig. S14 2D ^{13}C-^{13}C (10 kHz MAS) solid-state NMR spectra after the ^{13}C-methanol conversion over monofunctional c-FER (green), f-FER (blue), and bifunctional c-FER+Y_2O_3 systems for 15 minutes at 450 °C. Two different motifs, i.e., side-on (η^2:η^2) and end-on (η^1:η^1) conformations, of mobile methanol molecules, were distinguished over c-FER, while only end-on (η^1:η^1) conformations were dominant over f-FER and c-FER+Y_2O_3. Moreover, c-FER and f-FER show an adduct between methanol and SMS, which can not be seen on the bifunctional c-FER+Y_2O_3 system.

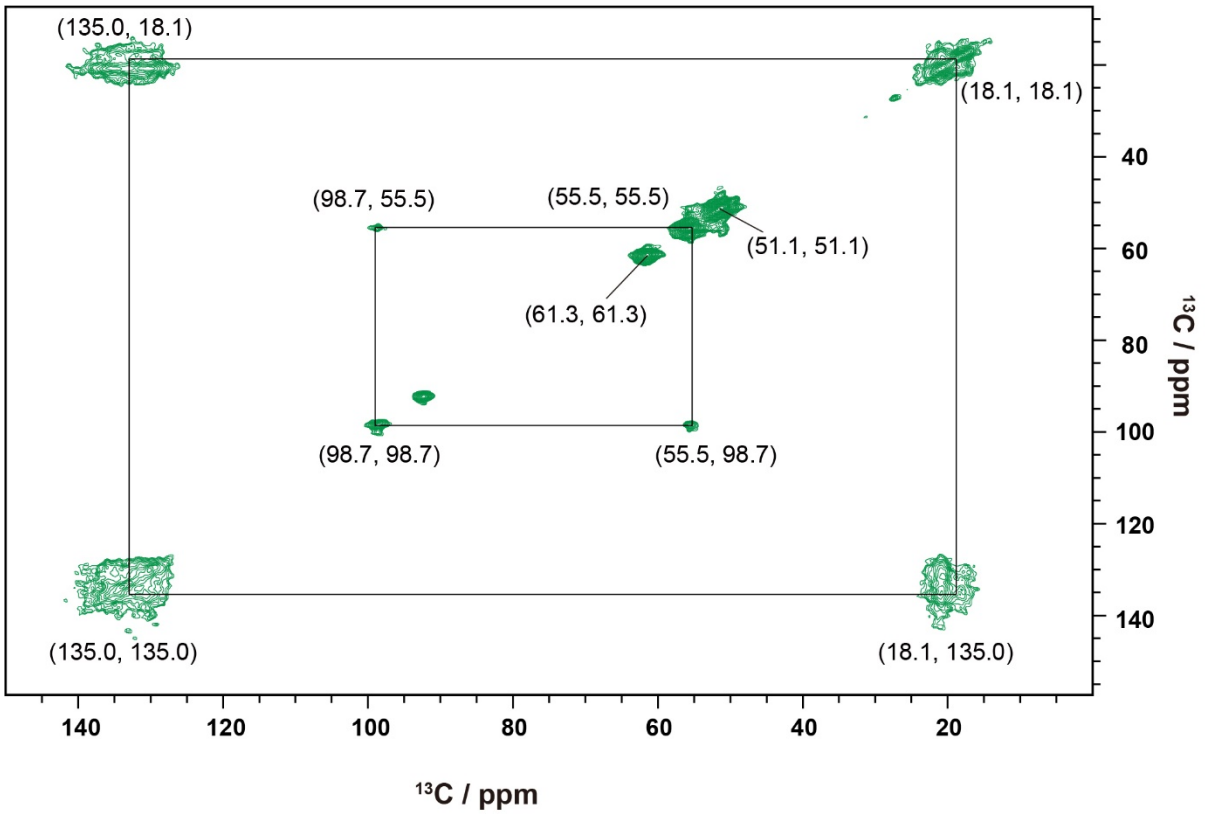

Fig. S15 2D ^{13}C-^{13}C (10 kHz MAS) solid-state NMR correlation spectrum of the post-reacted monofunctional c-FER zeolite. The sample was prepared after ^{13}C-methanol conversion over this catalyst at 450 ^{o}C for 15 min [magic angle spinning (MAS)].

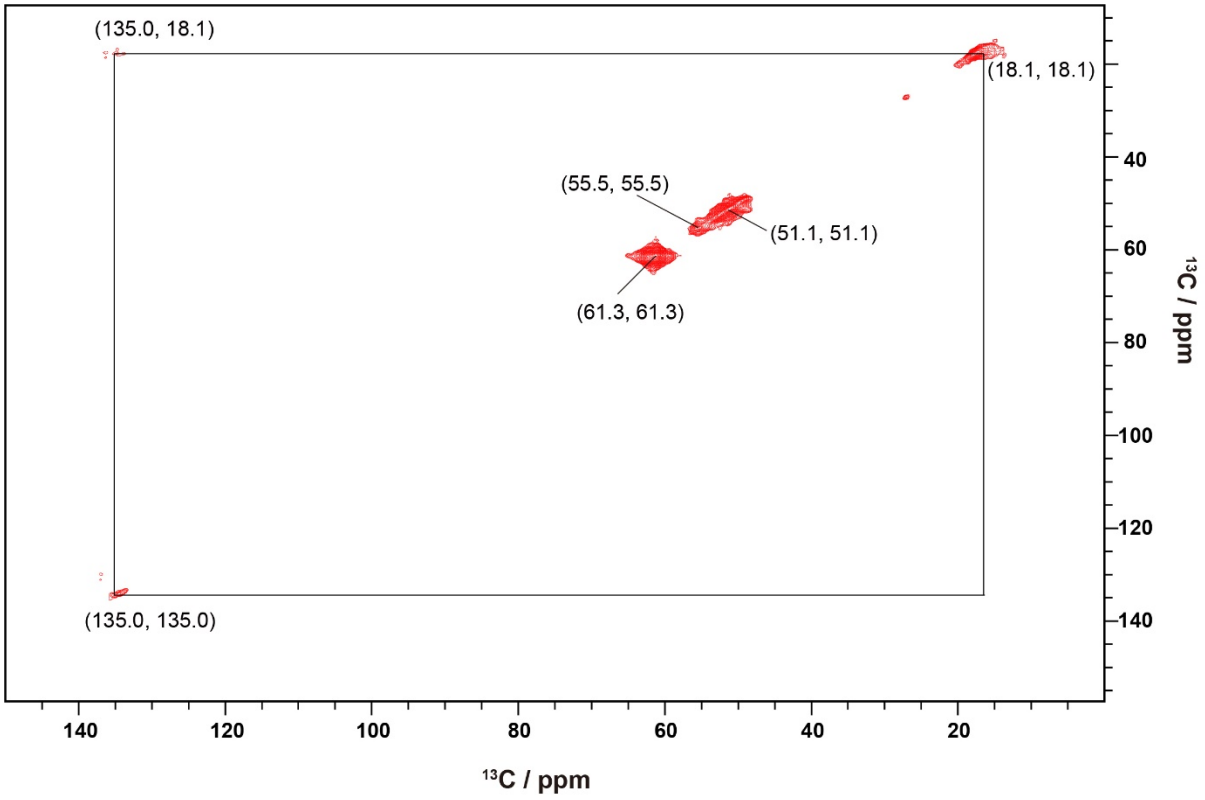

Fig. S16 2D ^{13}C-^{13}C (10 kHz MAS) solid-state NMR correlation spectrum of bifunctional c-FER+Y_2O_3 system. The sample was prepared after ^{13}C-methanol conversion over this catalytic system at 450 ºC for 15 min [magic angle spinning (MAS)].

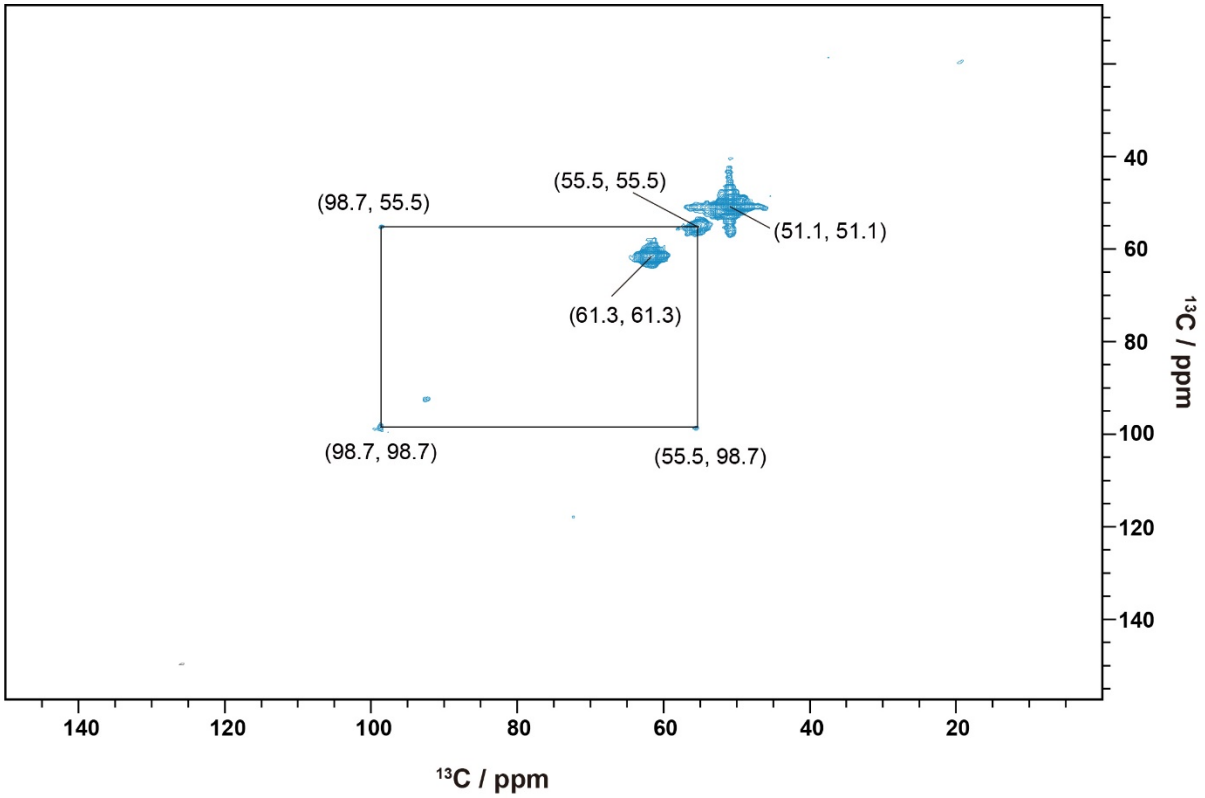

Fig. S17 2D ^{13}C-^{13}C (10 kHz MAS) solid-state NMR correlation spectrum of monofunctional f-FER zeolite. The sample was prepared after ^{13}C-methanol conversion over this catalyst at 450 ^{o}C for 15 min. [magic angle spinning (MAS)].

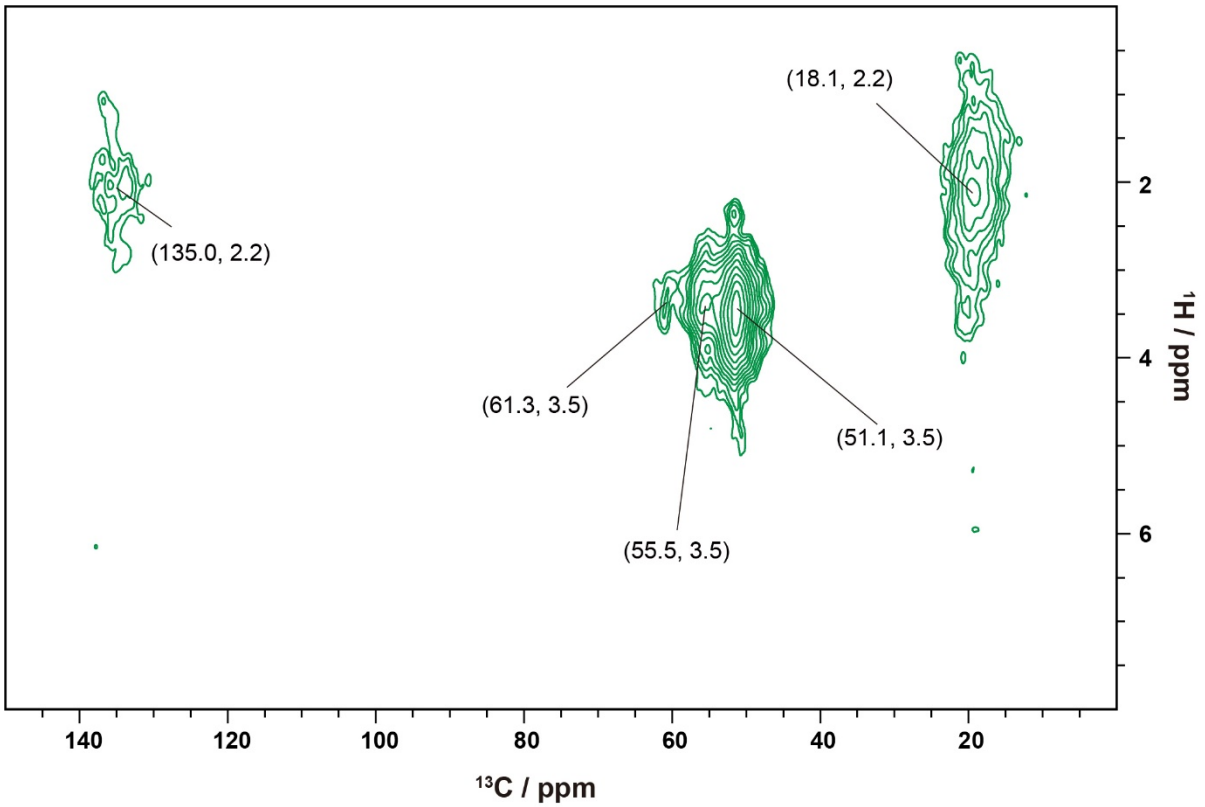

Fig. S18 2D ^{13}C-^{1}H (10 kHz MAS) solid-state NMR correlation spectrum of the monofunctional c-FER zeolite. The sample was prepared after ^{13}C-methanol conversion over this catalyst at 450 ºC for 15 min [magic angle spinning (MAS)].

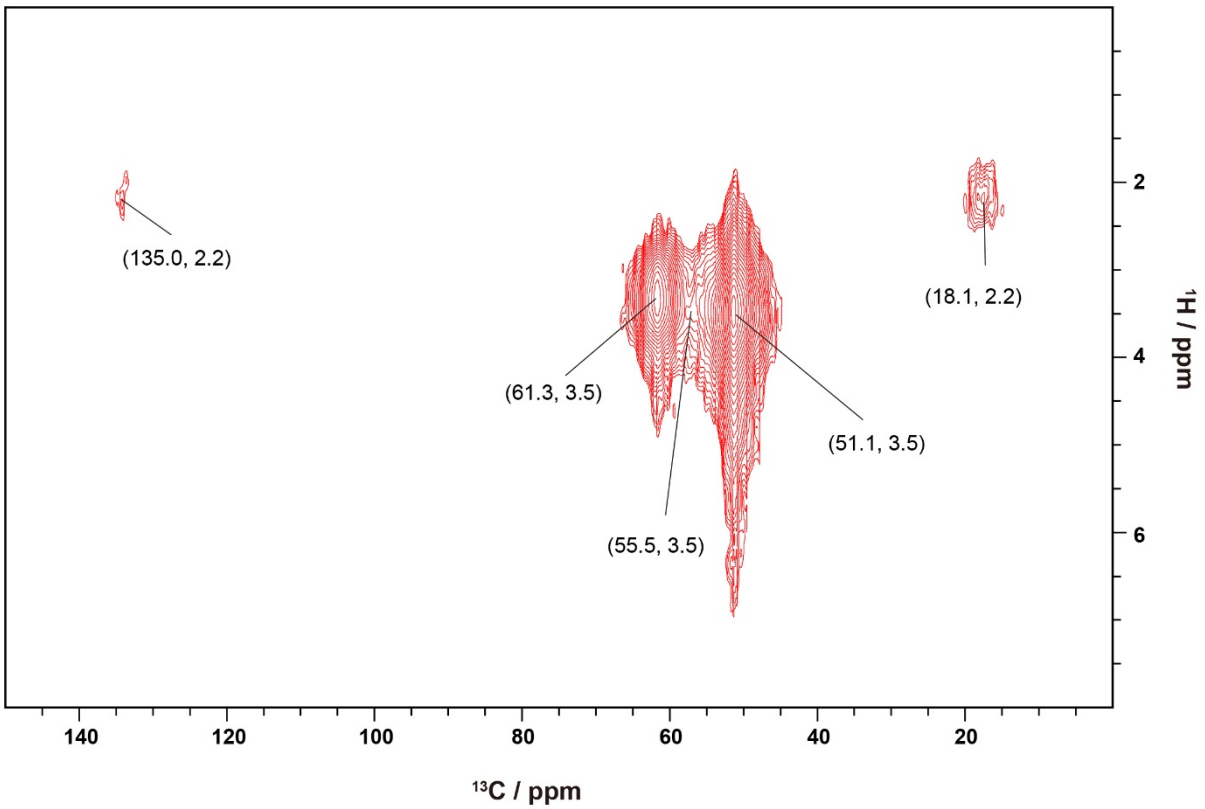

Fig. S19 2D ^{13}C-^{1}H (10 kHz MAS) solid-state NMR correlation spectrum of bifunctional c-FER+Y_2O_3 system. The sample was prepared after ^{13}C-methanol conversion over this catalytic system at 450 ºC for 15 min [magic angle spinning (MAS)].

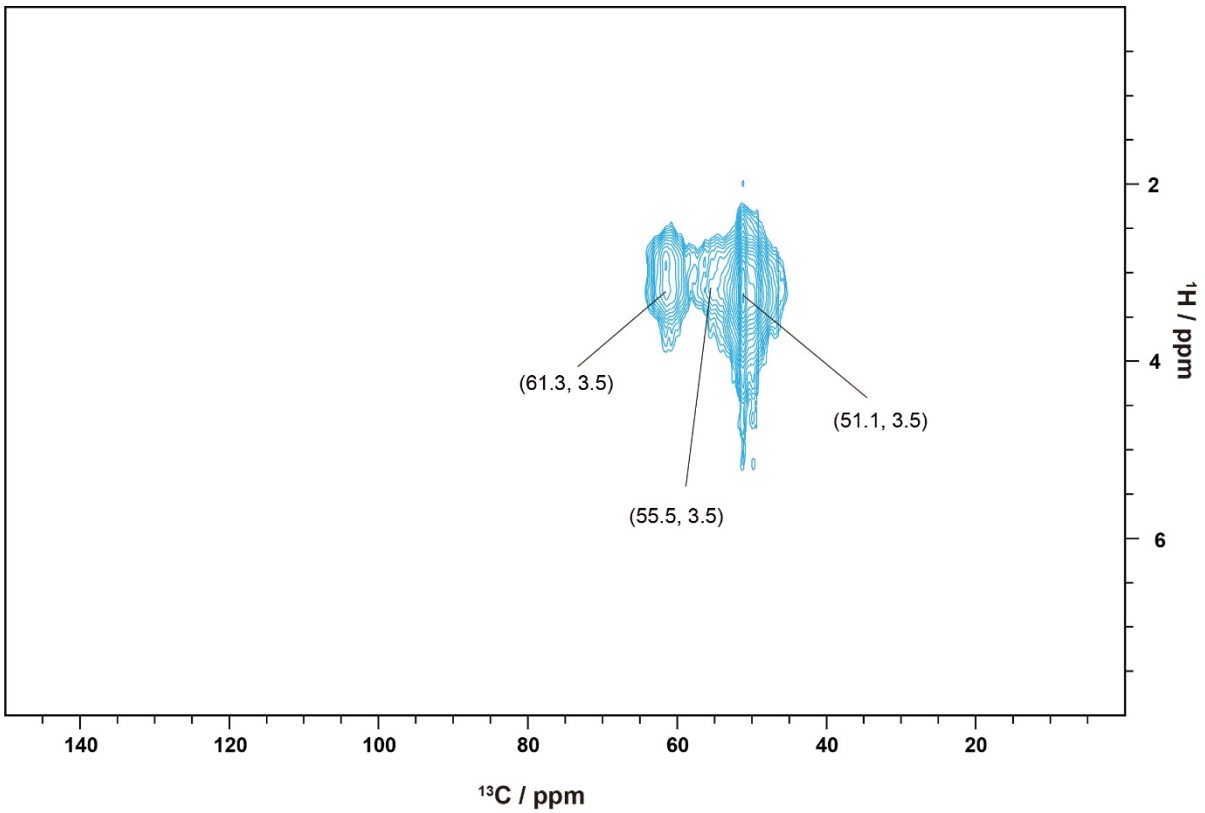

Fig. S20 2D ^{13}C-^{1}H (10 kHz MAS) solid-state NMR correlation spectrum of monofunctional f-FER zeolite. The sample was prepared after ^{13}C-methanol conversion over this catalyst at 450 ^{o}C for 15 min [magic angle spinning (MAS)].

Table S1. Acidity distribution of FER zeolites by NH_3-TPD

Samples	Acidity by strength (mmol·g^{-1})				Strong/ weak	Strong/ medium	Strong/ total
	Weak	Medium	Strong	Total			
c-FER	0.11	0.19	0.28	0.58	2.63	1.52	0.49
c-FER+Y_2O_3	0.13	0.22	0.24	0.59	1.83	1.10	0.41
f-FER	0.13	0.21	0.22	0.56	1.73	1.04	0.39

Table S2. Acid site quantification of zeolites via pyridine FTIR.

Samples	Acid sites detected at 150 °C (mmol/g)			Acid sites detected at 250 °C (mmol/g)		
	C_{BAS}	C_{LAS}	C_{BAS}/C_{LAS}	C_{BAS}	C_{LAS}	C_{BAS}/C_{LAS}
c-FER	0.24	0.11	2.28	0.18	0.06	3.12
f-FER	0.17	0.10	1.69	0.13	0.01	10.95

Table S3 A comparative literature summary involving FER zeolite catalyzed MTH process.

Materials	SAR	Temp. (ºC)	WHSV (h^{-1})	lifetime (h)	main products	selectivity (%)	Ref.
H-Ferrierite	n.r.[a]	450	1.08	n.r.	C_4-C_6	n.r.[a]	12
H-FER	20	400	1.2	0.1	C_5-C_6	35	13
Ce (10)-FER	20	400	1.2	1	C_4-C_6	80	13
Ce (20)-FER	20	400	1.2	>4	C_4-C_6	85	13
H-Ferrierite	20.3	400	1	<1	C_{4+}	40	14
H-ZSM-35	30	450	4	1	n.r.[a]	n.r.[a]	15
H-ZSM-35	28.6	300	2	n.r.[a]	C_5	45	16
H-Ferrierite	22	400	2	1	C_{4+}	60	17
c-FER	25	450	0.5	1	C_4-C_7	40	*This work*
c-FER+Y_2O_3	25	450	0.5	7	C_4-C_7	49	*This work*
f-FER	33.4	450	0.5	3	aromatics	32	*This work*
f-FER+Y_2O_3	**33.4**	**450**	**0.5**	**20**	**C_4-C_7**	**43**	***This work***

[a] n.r.: Not reported/mentioned/specified

S4. Supplementary References

1 S. Candamano, P. Frontera, T. I. Korányi, A. Macario, F. Crea and J. B. Nagy, Characterization of (Fe,Al)FER synthesized in presence of ethylene glycol and ethylene diamine, *Microporous Mesoporous Mater.*, 2010, **127**, 9–16.

2 S. Zhang, M. Cui, Y. Zhang, J. Zheng, T. Lv, W. Gao, X. Liu and C. Meng, Study on the synthesis of FER and SOD in the presence of ethylene glycol and the oxidation transformation of ethylene glycol in a confined region of zeolites, *J. Alloys Compd.*, 2017, **696**, 788–794.

3 C. A. Emeis, Determination of integrated molar extinction coefficients for infrared absorption bands of pyridine adsorbed on solid acid catalysts, *J. Catal.*, 1993, **141**, 347–354.

4 J. Valecillos, H. Vicente, A. G. Gayubo, A. T. Aguayo and P. Castaño, Spectro-kinetics of the methanol to hydrocarbons reaction combining online product analysis with UV–vis and FTIR spectroscopies throughout the space time evolution, *J. Catal.*, 2022, **408**, 115–127.

5 A. D. Chowdhury, K. Houben, G. T. Whiting, M. Mokhtar, A. M. Asiri, S. A. Al-Thabaiti, S. N. Basahel, M. Baldus and B. M. Weckhuysen, Initial Carbon–Carbon Bond Formation during the Early Stages of the Methanol-to-Olefin Process Proven by Zeolite-Trapped Acetate and Methyl Acetate, *Angew. Chem., Int. Ed.*, 2016, **55**, 15840–15845.

6 A. D. Chowdhury, A. L. Paioni, K. Houben, G. T. Whiting, M. Baldus and B. M. Weckhuysen, Bridging the Gap between the Direct and Hydrocarbon Pool Mechanisms of the Methanol-to-Hydrocarbons Process, *Angew. Chem., Int. Ed.*, 2018, **57**, 8095–8099.

7 W. Wen, S. Yu, C. Zhou, H. Ma, Z. Zhou, C. Cao, J. Yang, M. Xu, F. Qi, G. Zhang and Y. Pan, Formation and Fate of Formaldehyde in Methanol-to-Hydrocarbon Reaction: In Situ Synchrotron Radiation Photoionization Mass Spectrometry Study, *Angew. Chem., Int. Ed.*, 2020, **59**, 4873–4878.

8 Y. Liu, F. M. Kirchberger, S. Müller, M. Eder, M. Tonigold, M. Sanchez-Sanchez and J. A. Lercher, Critical role of formaldehyde during methanol conversion to hydrocarbons.,

Nat. Commun., 2019, **10**, 1462.

9 W. Wen, S. Yu, C. Zhou, H. Ma, Z. Zhou, C. Cao, J. Yang, M. Xu, F. Qi, G. Zhang and Y. Pan, Formation and Fate of Formaldehyde in Methanol-to-Hydrocarbon Reaction: In Situ Synchrotron Radiation Photoionization Mass Spectrometry Study, *Angew. Chem., Int. Ed.*, 2020, **59**, 4873–4878.

10 S. Müller, Y. Liu, F. M. Kirchberger, M. Tonigold, M. Sanchez-Sanchez and J. A. Lercher, Hydrogen Transfer Pathways during Zeolite Catalyzed Methanol Conversion to Hydrocarbons, *J. Am. Chem. Soc.*, 2016, **138**, 15994–16003.

11 A. Hwang and A. Bhan, Bifunctional Strategy Coupling Y2O3-Catalyzed Alkanal Decomposition with Methanol-to-Olefins Catalysis for Enhanced Lifetime, *ACS Catal.*, 2017, **7**, 4417–4422.

12 J. F. Haw, W. Song, D. M. Marcus and J. B. Nicholas, The mechanism of methanol to hydrocarbon catalysis, *Acc. Chem. Res.*, 2003, **36**, 317–326.

13 S. J. Park, H. G. Jang, K. Y. Lee and S. J. Cho, Improved methanol-to-olefin reaction selectivity and catalyst life by CeO2 coating of ferrierite zeolite, *Microporous Mesoporous Mater.*, 2018, **256**, 155–164.

14 S. Teketel, L. F. Lundegaard, W. Skistad, S. M. Chavan, U. Olsbye, K. P. Lillerud, P. Beato and S. Svelle, Morphology-induced shape selectivity in zeolite catalysis, *J. Catal.*, 2015, **327**, 22–32.

15 L. Qi, J. Li, L. Xu and Z. Liu, Evolution of the reaction mechanism during the MTH induction period over the 2-dimensional FER zeolite, *RSC Adv.*, 2016, **6**, 56698–56704.

16 M. Zhang, S. Xu, Y. Wei, J. Li, J. Chen, J. Wang, W. Zhang, S. Gao, X. Li, C. Wang and Z. Liu, Methanol conversion on ZSM-22, ZSM-35 and ZSM-5 zeolites: Effects of 10-membered ring zeolite structures on methylcyclopentenyl cations and dual cycle mechanism, *RSC Adv.*, 2016, **6**, 95855–95864.

17 S. C. Baek, Y. J. Lee, K. W. Jun and S. B. Hong, Influence of catalytic functionalities of zeolites on product selectivities in methanol conversion, *Energy and Fuels*, 2009, **23**, 593–598.